Solidification and fcc to metastable hcp phase transition in krypton under variable compression rates

Jing-Yin Chen,[1] Choong-Shik Yoo,[2] William J. Evans,[1] Hanns-Peter Liermann,[3] Hyunchae Cynn,[1] Minseob Kim,[2] and Zsolt Jenei[1]

[1]*Condensed Matter and Materials Division (CMMD), Physical & Life Science Directorate, Lawrence Livermore National Laboratory (LLNL), Livermore, California 94551, USA*

[2]*Department of Chemistry, Institute for Shock Physics, Washington State University, Pullman, Washington 99164, USA*

[3]*Photon Sciences, Deutsches Elektronen-Synchrotron (DESY), D-22603 Hamburg, Germany*

(Received 4 February 2014; revised manuscript received 14 September 2014; published 15 October 2014)

We present time-resolved synchrotron x-ray diffraction measurements to study kinetics associated with the liquid-solid and solid-solid high-pressure phase transitions in Kr under dynamic loading in a dynamic-diamond anvil cell. The results show a strong compression-rate dependence of the solidification/melting process in liquid Kr. The analysis of the compression-rate dependent melting/solidification, using an Avrami equation with the parameter $n = 1$, indicates a spontaneous nucleation and one-dimensional growth mechanism. In contrast, the face-centered-cubic to metastable hexagonal close-packed transition in solid Kr occurs rapidly at ∼0.8 GPa near the melting line, which has negligible compression-rate dependence within the range of compression rates studied (0.004–13 GPa/s).

DOI: 10.1103/PhysRevB.90.144104 PACS number(s): 62.50.−p, 81.40.Vw, 61.43.−j, 61.72.Dd

I. INTRODUCTION

Understanding the dynamic response of solids under extreme conditions of pressure, temperature, and strain rate is a fundamental scientific quest and a basic research need in materials science. Specifically, obtaining an atomistic description of structural and chemical changes of solids under rapid heating and/or compression over large temporal, spatial, and energy ranges is challenging but critical to understanding material stability or metastable structure, chemical mechanism, transition dynamic, and mechanical deformation. In this regard, developing time-resolved x-ray diffraction applied to solids under dynamic conditions is timely and synergistic to many proposed activities centered at third- and fourth-generation light sources.

Critical to high-pressure kinetic studies is the ability to precisely control pressure and compression rates over a wide range of governing time scales. Solid-state transformations under static high pressures are typically diffusion-limited, occurring in an intermediate time scale of microseconds to milliseconds and between those of conventional static (<1 GPa/s) and shock wave (>10^7 GPa/s) compressions. This is the time scale or compression rate that can be obtained, in a controlled way, using dynamic diamond anvil cells (dDAC) [1–5]. Hence, in this study, we combined dDAC with time-resolved synchrotron x-ray diffraction to probe structural evolutions and transition dynamics associated with melting and phase transitions of krypton under dynamic pressure loadings.

Noble gas liquids, with the exception of helium, crystalize into a face-centered-cubic (fcc) structure at low temperatures or at elevated pressures. Theoretical calculations [6,7], however, predict a diminishingly small energy difference as a function of pressure between fcc and hexagonal close-packed (hcp) structures in noble gas solids. In fact, a series of sluggish transitions have been found in fcc-Xe under pressures, first to an intermediate close-packed phase at ∼14 GPa, then to hcp above 75 GPa [8]. The sluggish nature of the transition in solid Xe often resulted in large stacking disorders in the fcc lattice and both fcc and hcp phases that were observed over a wide pressure range between 3 and 70 GPa after high temperature annealing by laser heating [9,10]. Xenon metallizes above 130 GPa [8,11,12], presumably in this high-pressure hcp phase. A similar fcc-to-hcp transition was also observed in laser-heated Kr at the pressure range of 3 to 50 GPa [13].

Electronic structure calculations [7] have suggested that the hybridization between the s/p and d bands favors the hcp structure of Xe at high pressures before it metallizes at ∼130–150 GPa [11,12]. However, because of the small energy difference between the fcc and hcp structures, it is difficult to depict the onset of the transition. The fcc-to-hcp transition in Kr, on the other hand, has been predicted to occur well above 130 GPa [14], substantially higher than the pressure range (3–50 GPa) previously observed [13]. This difference is likely due to the presence of shear in the sample that can introduce the stacking disorder well below the transition pressure.

The fcc structure has an ABC packing order along the body diagonal, while the hcp structure has an AB packing order along the c axis. Due to numerous slip systems in close-packed structures, imposition of shear or differential stresses can lead to a fcc-to-hcp transition, which is often observed in close-packed metals [15–18]. However, it is also important to note that the stacking disorder is not the only mechanism causing the fcc-to-hcp transition. The hcp structure, for example, has previously been observed upon the rapid solidification of laser-heated Kr at substantially lower pressures (below 50 GPa) [8–10]. As such, it appears to signify other mechanisms governing the transition including lattice defects and disorders.

In order to understand the fcc-to-hcp transition mechanism, we have investigated Kr under dynamic loadings in dDAC and measured the structural changes associated with the pressure-induced melting/solidification and fcc-to-hcp transitions in Kr over a wide range of compression rates. The present experiments have been performed at relatively low pressure at room temperature—in the range far from the predicted fcc-to-hcp transition but near the melting point, where the

formation of defects and stacking disorders can play significant roles depending on the compression rates.

II. EXPERIMENTS

High purity krypton gas (>99.995%, Alfa Aesar) was used without further purification. Kr was loaded cryogenically into a small hole (0.08–0.13 mm in diameter) of a preindented stainless steel gasket mounted between two opposed diamond anvils with 0.3 mm culets, together with a few small ruby spheres and copper powder for pressure estimation. Based on the microphotographic image and x-ray diffraction pattern, the loaded Kr shows no apparent trace of impurities.

Time-resolved x-ray diffraction experiments were carried out using monochromatic synchrotron x-rays at 25.7 keV (0.48262 Å) at the Extreme Conditions Beamline (ECB) P02.2 at Positron-Electron Tandem Ring Accelerator (PETRA) III, Deutsches Elektronen-Synchrotron (DESY). The incident x-ray beam was focused to a spot size of full width half-maximum, ~2 (H) × 7 (V) μm^2 using a compound refractive lens (CRL) system, and the two-dimensional (2D) diffraction pattern was collected using a Pilatus 1M area detector. Electronic instrumentation was used for synchronization, triggering, and monitoring the timing between the x-ray detector and dDAC, including a piezoactuator power amplifier, a function generator, a delay generator, and a digital oscilloscope.

For these studies, we utilized a dDAC, which adapts three piezoelectric actuators (Piezo Jenna) into a conventional DAC [19]. The loading profiles of the piezoelectric actuators, including peak pressure (P), pressure modulation (ΔP), compression rate ($\Delta P/\Delta t$), and load frequencies (f), are precisely controlled by the applied waveform of the electric drive signal, as shown in Fig. 1. The diagram shows the timing of a representative experiment, recorded by an oscilloscope, and includes the pressure modulation (black) and the feedback signal of the Pilatus detector (gray), in comparison to the measured pressure (solid circles) and sample lattice parameters (open diamonds). The arrows indicate when the trigger pulses were sent to the function generator and the detector. The sample pressure was estimated from the measured Cu (111) peak position using the equation of state (EOS) previously reported [20]. This is because the (111) reflection is the most dominant feature observed in all our diffraction data. We used three types of waveforms (sine, square, and trapezoid waves) to generate the pressure modulation across the liquid-solid transition. Note that there is a small time delay between the observed Cu and Kr pressure (or lattice) shifts. This delay originates from the difference in compressibility between Cu and Kr samples. The compression (or decompression) rate of the experiment is estimated by the rising (or falling) slope of the determined pressure versus time.

A series of x-ray diffraction images were collected with varying exposure times at the frequency range of 2 (500 ms x-ray exposure) to 33 (30 ms) Hz. Three selected diffraction images of one diffraction experiment are shown in Fig. 2(a).

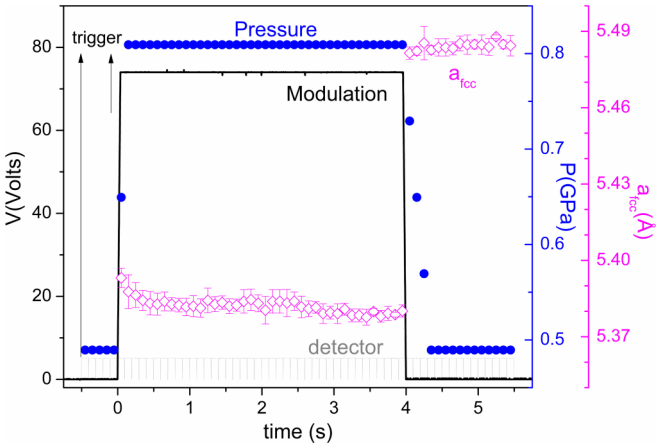

FIG. 1. (Color online) One representative applied waveforms (black line) into piezoactuators and the detector response (gray line) on the left vertical axis and the experimental pressures estimated from Cu (solid circles) and the lattice parameter of Kr-fcc (open diamonds) on the right vertical axes.

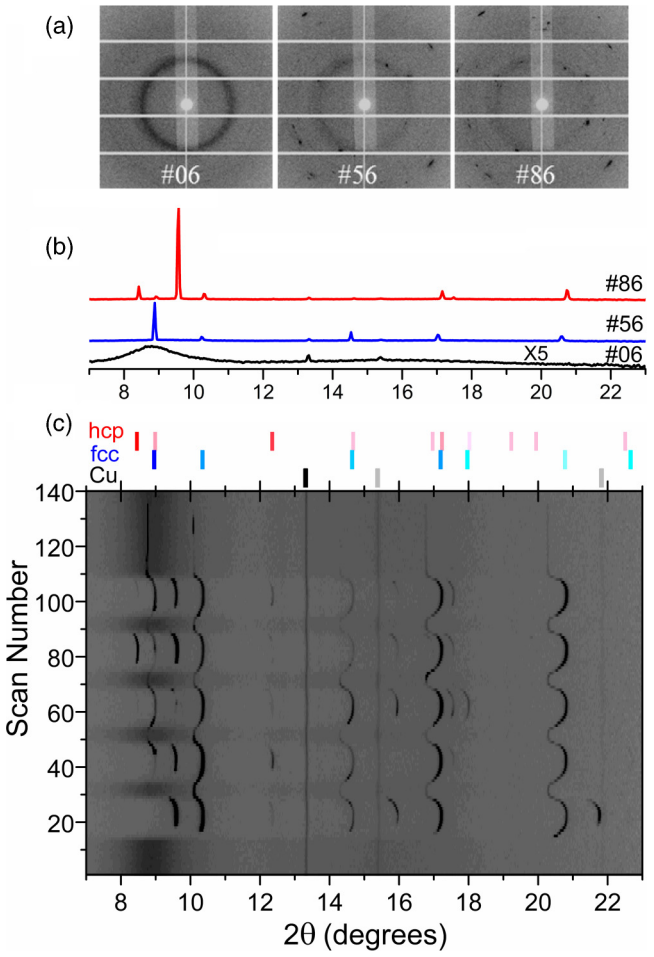

FIG. 2. (Color online) (a) Three representative diffraction images during the modulation. The number stated in the image is the scan number of the modulation. (b) The integrated diffraction patterns from the selected images. (c) A 2θ-scan_number plot of a series of time-resolved diffraction measurements with 50 ms exposure time, consisting of five consecutive, 1-s-long truncated sine wave pressure modulations and the calculated diffraction patterns of Cu (black), Kr-fcc (blue), and Kr-hcp (red) at 1.1 GPa.

We used the Fit2D program [21] to process the diffraction images and convert them to intensity versus 2θ plots [as shown in Fig. 2(b)] or a 2D contour plot to examine the lattice response to the pressure variation in Fig. 2(c). For comparison, the solid bars at the top of Fig. 2(c) represent the calculated peak positions for Cu and fcc- and hcp-Kr at 1.1 GPa using CrystalMaker. Figure 2(c) illustrates a series of dynamic loadings of Kr, consisting of five consecutive, 1-s-long truncated sine wave pressure modulations. Note that, at the beginning of the experiment, Kr is in the liquid state, solidifies into the fcc phase, and then transforms into a hcp structure during compression. Upon decompression, both the fcc and hcp phases melt, but only partially; a remnant of the fcc phase persists. During the five consecutive pressure modulations, not all of the diffraction peaks appear in each cycle. Some diffraction peaks appear and develop after a brief delay.

We analyzed the measured angle-resolved diffraction patterns in Fig. 2(b) using Jade (MDI, Jade 9) to index the diffraction peaks of Cu and the high-pressure polymorphs of Kr. Then we analyzed the spectral shape of each indexed peak using MATLAB to locate the peak position, the intensity at the peak center, and the integrated intensity of the peak for further kinetic analysis. The indexed peak positions give the lattice parameters for Cu, fcc-Kr, and hcp-Kr.

III. RESULTS

Krypton is initially in liquid state, as indicated by the first broad diffuse diffraction ring at around $2\theta = 9°$ illustrated in Fig. 3(a) and the very weak second broad diffraction ring located at $2\theta = \sim 15.5°$. The solidification process is studied by tracking the spectral changes on this broad liquid diffraction

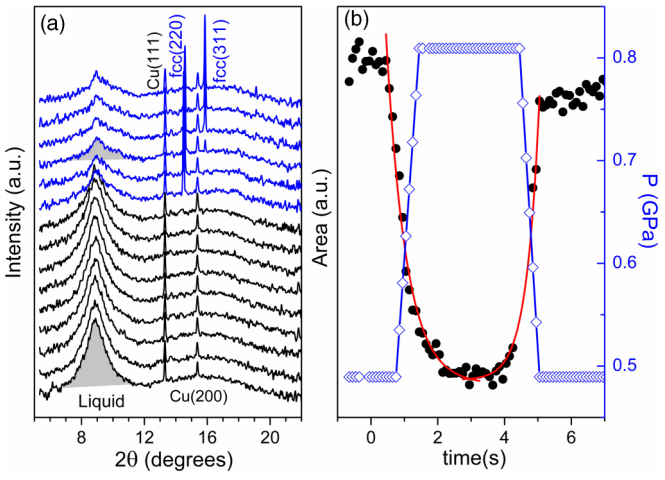

FIG. 3. (Color online) (a) A stacking plot of x-ray diffraction patterns between 5° and 15° during compression. A broad peak centered at 9° is the liquid diffuse peak, the peak at $2\theta = 13.5°$ is the Cu (111) diffraction peak and the peak at $2\theta = 14.7°$ is the Kr-fcc (220) diffraction peak. The gray area illustrates the integrated area of liquid Kr. (b) The integrated area of liquid Kr (solid circles) on the left vertical axis and the pressure (open diamonds) on the right vertical axis as a function of time. The red lines are the exponential fits.

line with pressure. The intensity of the broad liquid peak gets weaker, and the peak position shifts toward a slightly higher angle, as pressure increases. The change in the diffraction intensity, or the peak area calculated by integrating the area beneath the peak, is notable with the pressure change, as illustrated in Fig. 3(b). The integrated peak area (solid circles) and the measured pressure (open diamonds) are represented as a function of time of the pressure loading in Fig. 3(b). Note that liquid and solid Kr coexist over a small pressure range after the crystallization starts. This is due to the fact that the pressure increase stagnates at the transition pressure, and the driving peak pressure remains slightly lower than (or near) the equilibrium solidification pressure ~0.9 GPa.

The analysis shows that the peak area in Fig. 3(b) decreases (or increases) exponentially with time during the compression (or decompression) at the onset of solidification (or melting) of the Kr. This peak area change can be described in terms of a simple exponential decay/growth equation as represented in the red curves, $Y = 1 - a^* \exp(-t^n/\tau)$ where τ is the decay/growth time constant with $a = -0.676 \pm 0.04$, $\tau = 0.599 \pm 0.04$ s, and $n = 1$. This fact, a simple exponential equation represents the growth (nucleation) equation, indicates there is little contribution from pressure during solidification or melting once the dynamic pressure loading is enough to initiate the process. According to the Avrami equation [22], a simple exponential fit ($n = 1$) of the liquid-solid and solid-liquid transitions implies a homogeneous nucleation process, in which all nucleation occurs spontaneously in a supercooled (or supercompressed, in the present case) state and there is one-dimensional growth of solid/liquid (a rod-shaped product). This result probably reflects the hydrodynamic nature of dynamic pressure loading (or unloading) in the dDAC, which drives the Kr sample into a supercompressed (or undercompressed) state near the diamond-Kr interfaces while the mean pressure still remains unchanged. Based on the data in Fig. 3, we estimate that the Kr sample at the interfacial region is supercompressed by ~0.3 to 0.8 GPa, sufficient to initiate the solidification process at the mean pressure of 0.5 GPa.

In Fig. 4, we present the solidification or melting time constant defined as τ from the exponential fit as a function of compression (solid circles) or decompression (open circles) rates. As expected, the solidification (or melting) time constants increase as the compression (or decompression) rate decreases (Fig. 4). Note that they follow a linear relationship in the logarithmic plot (Fig. 4 inset) with a slope of 0.72 (± 0.06) GPa^{-1} for the solidification and 0.63 (± 0.2) GPa^{-1} for the melting. This indicates a similar mechanism governing both the crystallization and melting. A similar linear relationship between the compression rate and the growth rate has often been observed in other solid-solid transformations [22–23]. The slope is related to the activation energy, yet the time resolution of the experiments in this paper is not sufficient to resolve the transition pressure to extract activation energy, based on the transition state model [24].

Figure 5 shows contour plots of 2θ-time of diffraction patterns obtained under three different dynamic loadings with the compression rates of (a) ~8 GPa/s (50 ms exposure), (b) 1.9 (± 0.1) GPa/s (200 ms exposure), and (c) 0.005 (± 0.001) GPa/s (500 ms exposure). The calculated diffraction

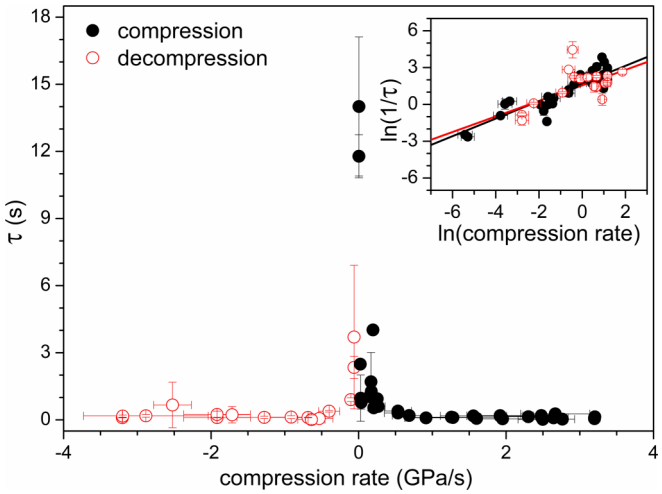

FIG. 4. (Color online) The decay/growth time constants τ (solid circles: compression, open circles: decompression) across the liquid-solid phase boundary as a function of compression rates in a linear scale and in a natural logarithmic scale (inset). The black line is the linear fit of the data during compression, and the red line is the linear fit of those during decompression.

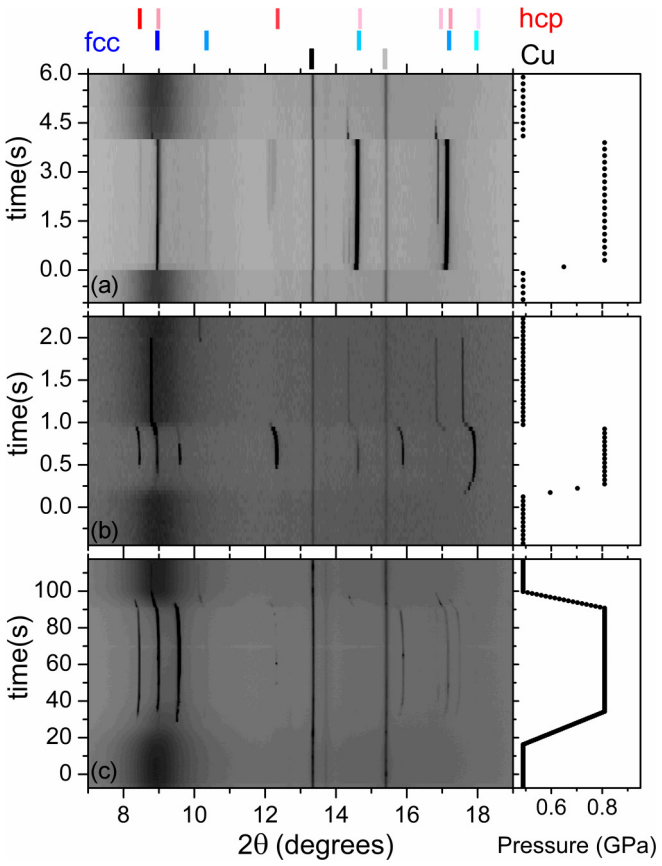

FIG. 5. (Color online) Three representative 2D 2θ-time plots of time-resolved diffraction pattern (with a trapezoidal wave pressure modulation) at (a) faster ~8 GPa/s (50 ms exposure), (b) moderate 1.9 (±0.1) GPa/s (200 ms exposure), and (c) slower 0.005 (± 0.001) GPa/s (500 ms exposure) compression rates with its measured pressure (solid circles) and the bars showing the calculated diffraction patterns of Cu (blacks), Kr-fcc (blues), and Kr-hcp (reds) at ~1.1 GPa.

peak positions are also marked as vertical bars at the top: Cu (in black bars), fcc-Kr (in blue), and hcp-Kr (in red) at 1.1 GPa, as well as the measured pressure at the right of the figure. Note that there is a time delay during decompression between the initial pressure decreases as estimated by Cu EOS and the start of the shift of the diffraction peaks of Kr. This discrepancy is due to the difference in compressibility of Cu and Kr.

Upon the fast compression at 8 GPa/s in Fig. 5(a), the fcc phase of Kr appears nearly instantaneously as the pressure increases, while a hcp phase appears after a delay of ~1 s. The presence of the hcp is apparent from the appearance of at least three diffraction peaks (100), (102), and (200) with 2θ values of 8.46, 12.2, and 16.9, respectively. Note that the (102) peak appears as a doublet, which likely represents stacking disorder in this metastable hcp-phase. In addition to the existence of metastable hcp, there are two unidentified diffraction peaks, appearing 0.2 s after the pressure increases at $2\theta \sim 14.7°$. These two weak diffraction peaks diminished with time and are most likely related to the growth of the hcp diffraction peaks. Since no other peaks are possibly related to the hcp phase and the intensity changes of these two peaks at 14.7° correspond to the later development of a doublet of metastable hcp (102) peak, all of these peaks may indicate a presence of a stacking-disordered intermediate phase as a precursor to the hcp phase. It is possible to observe more disordered peaks or no peaks (indicating amorphous or plastic solid) when the compression rates are increased further. Additional high compression rate experiments with better time resolution are needed to clarify the plausibility of this mechanism. Solid Kr starts to melt as soon as the pressure decreases. As expected, the hcp disappears first, then the fcc about 1 s later. During the largest compression rate experiment of this study, the hcp diffraction peaks are all very weak, implying that faster compression/decompression suppresses the formation of the hcp phase. In addition, the nucleation time of the fcc phase is much faster than that of the hcp phase at the higher compression rates.

At the intermediate compression rate of 1.9 GPa/s depicted in Fig. 5(b), the fcc phase appears first during the compression period (or above 0.6 GPa) as is evident from several sharp diffraction peaks including (111) at 8.9° and (222) at 17.7°; then the hcp phase starts to appear as the pressure reaches its peak pressure, as is evident from the (100), (101), (102), and (103) diffraction lines at ~8.4°, 9.6°, 12.3°, and 15.9°, respectively. Upon decompression, the hcp phase disappears as soon as liquid Kr starts to appear, whereas the fcc phase remains and coexists with liquid for at least 1 s. This reflects the metastable nature of the hcp phase, which converts immediately back to the fcc phase or the melt as the stacking disorder immediately dissipates upon melting.

At a compression rate of 0.005 GPa/s in Fig. 5(c), for example, there exists a large time delay between the sample response and the pressure modulation, ~9.7 s based on liquid Kr and ~16.2 s based on Cu. This delay accounts for the late decrease of the area of the liquid ~20 s after the pressure increase ($P \sim 0.6$ GPa). Surprisingly, the hcp-Kr appears at ~29 s after the pressure change and dominates the solid phase. At ~33 s, the (111) peak of the fcc-Kr appears, which could also be interpreted as the (002) of the hcp-Kr. Furthermore, the remaining diffraction peaks associated with fcc-Kr are very weak, including (200), (220),

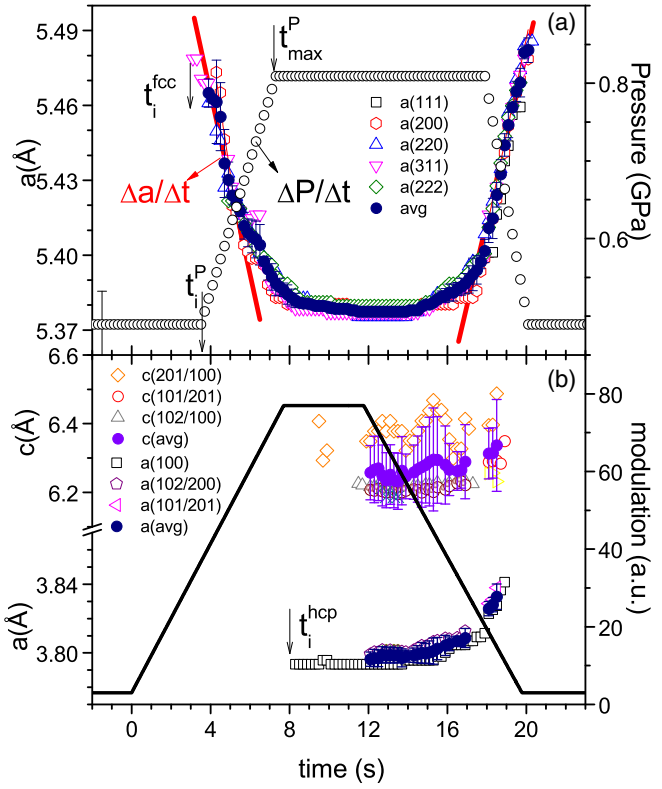

FIG. 6. (Color online) (a) Lattice parameter of Kr-fcc (symbols, left vertical axis) and pressure (open circles, right vertical axis) as a function of time. Different open symbols represent the lattice parameter calculated from different diffraction peaks and the average of lattice parameter shows in solid circles. (b) Lattice parameters of Kr-hcp (symbols, left vertical axis) and modulation waveform (black curves, right vertical axis) as a function of time. Different open symbols represent the lattice parameter calculated from different diffraction peaks and the averages of lattice parameters show in solid circles.

and (311) at 10.3°, 14.6°, and 17.1°, respectively. The fact that the hcp-Kr dominates at the slower dynamic loading implies that the kinetic energy favors the formation of hcp-Kr. A plausible explanation for the formation of the hcp-Kr phase when the compression rates are smaller than 0.005 GPa/s is that the formation of defects and stacking faults are much easier when the pressure compression rates are too low to form the equilibrium fcc phase. At slow compression rates, the transition to fcc is somewhat limited by a relatively high activation barrier with respect to the driving force and, instead, produces defects and stacking faults in the structure which require smaller formation energies.

Upon decompression, solid Kr expands first and then melts. During the melting process, the hcp-Kr disappears first, and then the fcc melts at all compression rates. Interestingly, at this slow dynamic loading, the amount of the fcc-Kr seems to increase first [~10% for (111) peak and 5% for (311)] before it converts to liquid. This may be due to the conversion of the hcp-Kr into the fcc-Kr (not to the melt).

Figure 6 shows the lattice parameter changes of (a) fcc- and (b) hcp-Kr upon the pressure modulations at the compression rate of 0.02 (±0.009) GPa/s, including both the lattice parameters from individual (*hkl*) planes (open symbols) and the average values (solid symbols). The compression rate $\Delta P/\Delta t$ is estimated from the slope of pressure change from the measured Cu (111) diffraction line using the previously reported equation of state [20]. The $\Delta a/\Delta t$ of the fcc phase, on the other hand, is obtained from the linear slopes of the lattice changes (red lines) during compression and decompression. The $t_i^{\rm fcc}$ (or $t_i^{\rm hcp}$) denote the time when the first fcc (or hcp) diffraction peak appears, whereas the t_i^P (or $t_{\rm max}^P$) denote the time when the pressure starts to increase (or reaches its maximum value). A delay between the sample responses and the modulation is observed, partially due to the delay of mechanical engagement of the piezo transducers and partially from the different sensitivities of Cu and Kr as described below. The large error bars on the calculated pressure compared to those of the calculated lattice parameters of Kr reflect the substantially greater compressibility of Kr phases in contrast to Cu. However, a systematic analysis allows meaningful comparisons among different dynamic loadings.

IV. DISCUSSION

The volumes of fcc and hcp-Kr as a function of time/t_m (t_m is the duration for one modulation) are presented in Figure 7(a). During dynamic loading, a ~2% volume compression (or decompression) is achieved. Clearly, the volumes of the fcc phase measured at different compression rates are in excellent agreement with each other. The volume of the hcp phase deviates slightly from that of the fcc when it initially forms, but it becomes the same during the decompression.

Note that there is a subtle difference in the measured volumes of the hcp phase at different compression rates; for example, those at 0.02 GPa/s compression rate are slightly larger than those at 0.07 and 1.9 GPa/s rates. The former agree well with the specific volumes of the fcc phase. This is interesting, because the metastable hcp phase becomes denser (by about 2%) than the stable fcc phase over the pressure range between 0.5 and 2 GPa, especially at the faster rate of compression. Nevertheless, it is consistent with a previous result [13], indicating that hcp-Kr, formed after laser-heating at high pressures of 20 GPa, is about 1.4% denser than the fcc phase. Although the volume difference between the hcp and fcc phases is well within the error bar, this observation may be related to the fact that the amount of hcp-Kr dominates at slower dynamic loadings, discussed above. The c/a ratios of the hcp-Kr measured at different dynamic loadings [in Fig. 7(a) inset] show a relatively large range of 1.60 to 1.68—reflecting a kind of stacking disorder in the hcp phase.

In Fig. 7(b), we summarize the average volume compression curves of the fcc (solid circles) and hcp (open circles) phases in comparison with those previously measured in static (solid line) and laser-heating (solid and open diamonds) experiments [10,13], in the pressure range of 0.5–2 GPa. The volume data of Kr are the average value of all volume data at the same measured pressure for all measurements. The scattering experimental data in the range of 0.5 and 1.1 GPa imply that the hysteresis during the pressure cycling are observed for both fcc-Kr and hcp-Kr phases, which is demonstrated by the selected sets of measurements shown in the inset of Fig. 7(b). The hysteresis loop of the fcc phase is slightly larger than that of the hcp phase. At higher pressure

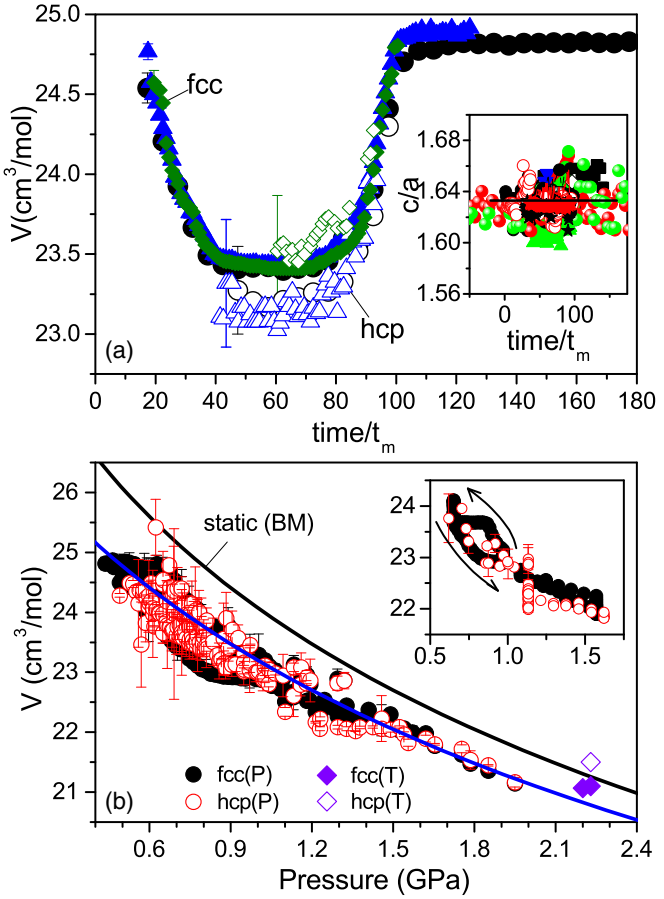

FIG. 7. (Color online) (a) Volumes of Kr-fcc (solid symbols) and Kr-hcp (open symbols) at three representative dynamic loadings (1.9 ± 0.1 GPa/s: circles, 0.07 ± 0.03 GPa/s: triangles, and 0.02 ± 0.009 GPa/s: diamonds) as a function of relative time, time/t_m (t_m: the modulation period). The inset plots the c/a ratios of Kr-hcp at all dynamic loadings as a function of time/t_m. The black line in the inset locates the ideal c/a ratio of hcp, 1.633. (b) Volumes of Kr-fcc (solid) and Kr-hcp (open) at dynamic loadings, volumes of fcc at static condition (curves), and volumes of fcc and hcp under laser-heating conditions (diamonds) as a function of pressure. The static P-V curve is calculated from the third-order Birch-Murnaghan equation [13]. The volumes of fcc and hcp are obtained from the previous laser-heating experiments [10]. The inset shows the representative hysteresis of fcc and hcp during compression (bottom) and decompression (top).

(>1.1 GPa), the hysteresis is below the sensitivity of our detection for both phases. The static compression curve is produced using the third-order Birch-Murnaghan (B-M) EOS with the previously reported parameters of the isothermal bulk modulus ($K_T = 2.7$ GPa), its first derivative with respect to pressure ($K' = 5.4$), and the volume at ambient condition ($V_0 = 29.7\,\mathrm{cm}^3$/mol) [13]. Again, the measured volumes of the hcp phase are very similar to those of the fcc, consistent with the coexistence of hcp and fcc. It also shows a subtle yet notable slope change in the pressure-volume curve at ~0.9 GPa—the previously reported solidification pressure [13]. Note that the extrapolation of the present compression curve agrees well with the previously observed volumes of the fcc (solid diamonds) and hcp (open diamond) phases

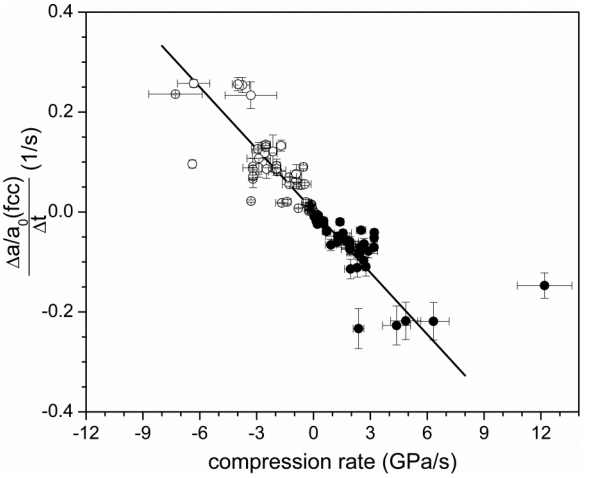

FIG. 8. The measured strain rate ($\Delta a/a_o/\Delta t$) of Kr-fcc as a function of compression rates. The solid circles are calculated under compression and the open circles are under decompression. The black line is the linear fit of the measured strain rates and compression rates.

under temperature modulation at ~2.2 GPa [10]. Nevertheless, the dynamic EOS agrees well with the static EOS within the pressure difference by 0.3 GPa, as shown by the blue curve.

The measured strain rate ($\Delta a/a_o/\Delta t$) decreases linearly from +0.4/s to −0.4/s as the compression rates increases from −9 to 12 GPa/s, as shown in Fig. 8. As such, the present result demonstrates the elastic response of the fcc lattice under dynamic loading. The slope of the fcc lattice change rate $\Delta a/\Delta t$ is −0.24(±0.01) Å/GPa. In fact, the measured linear compressibility ~0.041(±0.002) GPa^{-1} is calculated by dividing $a_0 = 5.8213$ Å from V_0 of B-M EOS [13]. Based on the reasonable assumption that fcc is isotropic, the isothermal compressibility ~0.123 (±0.006) GPa^{-1} in this study is quite similar to the isothermal compressibility of fcc-Kr, 0.167 GPa^{-1}, derived from the adiabatic bulk modulus ($Ks =$ 6 GPa at 1 GPa) of Kr from energy-dispersive x-ray diffraction and Brillouin scattering [25]. Hence, based on this observation, we conclude that the formation of the hcp phase is indeed induced by a simple stacking disorder of the fcc phase, not by the plastic deformation or twinning. A higher compression rate and/or higher pressure may be required to induce the plastic deformation of the fcc phase.

The induction times for the nucleation of the fcc and hcp phases can be estimated statistically as illustrated in Fig. 9. According to the Gaussian probability density function and the Gaussian fits shown in red, approximately 68% of the fcc phase nucleates and appears within −0.12–0.18 s from the instance of the pressure increase. In addition, approximately 68% of hcp-Kr appears in the timeframe of −0.28–0.57 s after the pressure reaches the peak value. The times of t_i^{fcc}, t_i^P, t_i^{hcp}, and t_{max}^P are defined in Fig. 6. The number of measurements used for the fcc and hcp phases are, respectively, 51 and 40. The threshold transition pressure of the hcp phase is found to be ~0.8 GPa at the compression rates ranging from 0.004 to 13 GPa/s, as shown in the inset. Even though the time resolutions of the current studies are slow, the induction times of this paper provide valuable information for future studies. In this paper, the induction times of fcc and hcp phases have no

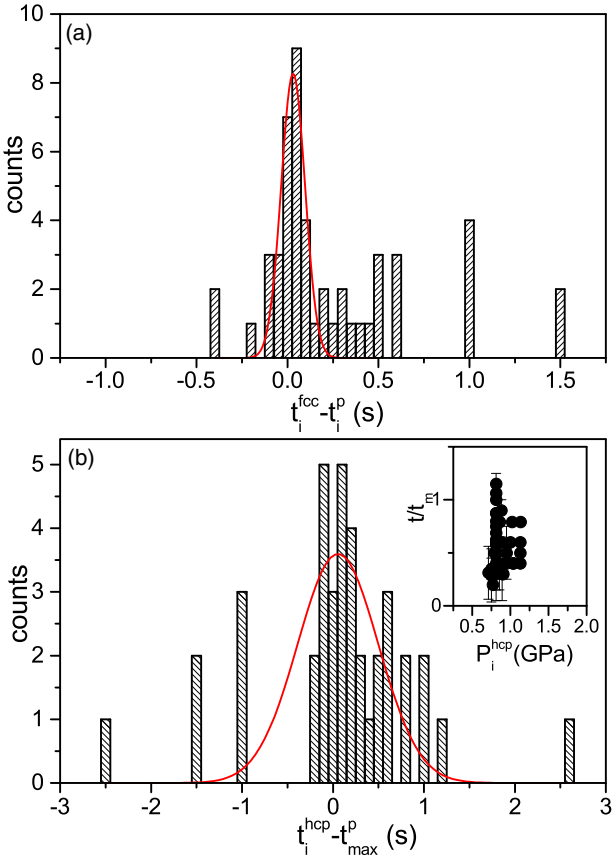

FIG. 9. (Color online) (a) The histogram of the time difference between when Kr-fcc first appears and when pressure starts to increase. (b) The histogram of the time difference between when Kr-hcp first appears and when pressure reaches the peak pressure. The red curves are the Gaussian fits, and the inset of the bottom panel illustrates the threshold pressures when Kr-hcp appears.

compression rate dependence or are not quantifiable because of the inadequate time resolution of our measurements. This result agrees very well with the observation of spontaneous nucleation observed in liquid Kr.

V. CONCLUSIONS

The solidification of Kr occurs through spontaneous nucleation of an fcc lattice, following a simple exponential decay of liquid Kr and the critical nucleation time of −0.12–0.18 s. Based on the Gaussian probability density analysis, the nucleation time of solid Kr is found to be independent of the compression rate over 0.004–13 GPa/s. The fcc lattice behaves elastically at all pressures and compression rates studied, which transforms into the metastable hcp phase at ∼0.8 GPa. We found that the formation of hcp-Kr is most pronounced at the slowest compression rates (<0.005 GPa/s), suggesting a defect-assisted transition mechanism. As such, the slow compression rate produces a larger amount of defects in the fcc lattice, which can lower the transition barrier to the hcp phase under dynamic compressions. Consequently, the formation of the metastable hcp at low pressure under dynamic loading confirms the predicted small volume difference between fcc and hcp phases. The isothermal compressibility ∼0.123 (±0.006) GPa^{-1} measured in this paper agrees reasonably well with the 0.167 GPa^{-1} previously obtained from the energy-dispersive x-ray diffraction and Brillouin scattering [25]. The measured linear strain rate of the fcc phase supports the suggestion that the fcc-to-hcp transition arises from stacking disorder in the fcc phase, not by the plastic deformation or twinning.

ACKNOWLEDGMENTS

This work at LLNL was performed under the auspices of the US Department of Energy under Contracts No. W-7405-Eng-48 and No. DE-AC52-07NA27344 and supported by the Laboratory Directed Research and Development Program under Project Tracking Code 11-ERD-046. The work at Washington State University was performed in support of the National Science Foundation Division of Materials Research (Grant No. 1203834) and the Defense Threat Reduction Agency (HDTRA1-12-01-0020). We appreciate Ken Visbeck at LLNL for his assistance in sample preparations. The x-ray studies were performed at the light source PETRA III at DESY, a member of the Helmholtz Association (HGF).

[1] G. W. Lee, W. J. Evans, and C. S. Yoo, Phys. Rev. B **74**, 134112 (2006).
[2] G. W. Lee, W. J. Evans, and C. S. Yoo, Proc. Nat. Acad. Sci. USA **104**, 9178 (2007).
[3] J.-Y. Chen and C. S. Yoo, Proc. Nat. Acad. Sci. USA **108**, 7685 (2011).
[4] J.-Y. Chen and C. S. Yoo, J. Chem. Phys. **136**, 114513 (2012).
[5] D. Tomasino and C. S. Yoo, Appl. Phys. Lett. **103**, 061905 (2013).
[6] M. Ross and A. K. McMahan, in *Physics of Solids Under High Pressure*, edited by J. S. Schilling and R. N. Shelton (North-Holland, Amsterdam, 1981), p. 161.
[7] A. K. McMahan, Phys. Rev. B **33**, 5344 (1986).
[8] A. P. Jephcoat, H.-k. Mao, L. W. Finger, D. E. Cox, R. J. Hemley, and C.-s. Zha, Phys. Rev. Lett. **59**, 2670 (1987).
[9] W. A. Caldwell, J. H. Nguyen, B. G. Pfrommer, F. Mauri, S. G. Louie, and R. Jeanloz, Science **277**, 930 (1997).
[10] H. Cynn, C. S. Yoo, B. Baer, V. Iota-Herbei, A. K. McMahan, M. Nicol, and S. Carlson, Phys. Rev. Lett. **86**, 4552 (2001).
[11] K. A. Goettel, J. H. Eggert, and I. F. Silvera, Phys. Rev. Lett. **62**, 665 (1989).
[12] R. Reichlin, K. E. Brister, A. K. McMahan, M. Ross, S. Martin, Y. K. Vohra, and A. L. Ruoff, Phys. Rev. Lett. **62**, 669 (1989).
[13] D. Errandonea, B. Schwager, R. Boehler, and M. Ross, Phys. Rev. B **65**, 214110 (2002).
[14] I. Kwon, L. A. Collins, and J. D. Kress, Phys. Rev. B **52**, 15165 (1995).
[15] R. Boehler, M. Ross, P. Söderlind, and D. B. Boercker, Phys. Rev. Lett. **86**, 5731 (2001).
[16] P. Tolédano, G. Krexner, M. Prem, H.-P. Weber, and V. P. Dmitriev, Phys. Rev. B **64**, 144104 (2001).

[17] D. A. Young, *Phase Diagrams of the Elements* (University of California Press, Berkeley, 1991).
[18] R. Bruinsma and A. Zangwill, Phys. Rev. Lett. **55**, 214 (1985).
[19] W. J. Evans, C. S. Yoo, G. W. Lee, H. Cynn, M. J. Lipp, and K. Visbeck, Rev. Sci. Instrum. **78**, 073904 (2007).
[20] Y. Wang, J. Zhang, H. Xu, Z. Lin, L. L. Daemen, Y. Zhao, and L. Wang, Appl. Phys. Lett. **94**, 071904 (2009).
[21] A. P. Hammersley, S. O. Svensson, M. Hanfland, A. N. Fitch, and D. Hausermann, High Pressure Res. **14**, 235 (1996).
[22] M. Avrami, J. Chem. Phys. **8**, 212 (1940).
[23] J. J. Jonas, X. Quelennec, L. Jiang and T. Martin, Acta Mater. **57**, 2748 (2009).
[24] M. G. Evans and M. Polanyi, Trans. Faraday Soc. **31**, 875 (1935).
[25] A. Polian, J. M. Besson, M. Grimsditch, and W. A. Grosshans, Phys. Rev. B **39**, 1332 (1989).